

ARTICLE OPEN



Anomalous valley Hall effect in antiferromagnetic monolayers

Wenhui Du¹, Rui Peng¹, Zhonglin He¹, Ying Dai¹✉, Baibiao Huang¹ and Yandong Ma¹✉

Anomalous valley Hall (AVH) effect is a fundamental transport phenomenon in the field of condensed-matter physics. Usually, the research on AVH effect is mainly focused on 2D lattices with ferromagnetic order. Here, by means of model analysis, we present a general design principle for realizing AVH effect in antiferromagnetic monolayers, which involves the introduction of nonuniform potentials to break of PT symmetry. Using first-principles calculations, we further demonstrate this design principle by stacking antiferromagnetic monolayer MnPSe_3 on ferroelectric monolayer Sc_2CO_2 and achieve the AVH effect. The AVH effect can be well controlled by modulating the stacking pattern. In addition, by reversing the ferroelectric polarization of Sc_2CO_2 via electric field, the AVH effect in monolayer MnPSe_3 can be readily switched on or off. The underlying physics are revealed in detail. Our findings open up a new direction of research on exploring AVH effect.

npj 2D Materials and Applications (2022)6:11 ; <https://doi.org/10.1038/s41699-022-00289-6>

INTRODUCTION

Valley, characterizing energy extrema of conduction or valence band, is an emerging degree of freedom of carriers in condensed-matter materials^{1,2}. Benefiting from the large separation in momentum space, the valley degree of freedom is particularly stable against low-energy phonons and smooth deformations^{3–5}. Analogous to charge and spin, the valley degree can be utilized to encode information and perform logic operations, leading to the concept of valleytronics^{6,7}. Early interest in valley dates back to the works in 1970s on silicon inversion layer^{8,9}. In recent years, following the discoveries of intrinsic physical properties associated with valley occupancy in two-dimensional (2D) lattices^{10,11}, rapid experimental and theoretical progress^{12–46} has been made in the field of valleytronics at both the fundamental and applied levels.

As a new piece of puzzle in the Hall family, the anomalous valley Hall (AVH) effect in valley-polarized materials lies at the heart of valleytronics. In principle, polarized light is able to induce AVH effect in valley-polarized monolayers, however, it is a dynamic process and subjected to the life time of carriers, which is not applicable for practical valleytronics^{27,28}. Physically, there are two essential ingredients for realizing stable AVH effect: one is magnetism and the other is spin-orbital coupling (SOC), which, respectively, plays the role of breaking the time-reversal symmetry and giving rise to coupled spin and valley physics. The former can be either intrinsic magnetism^{29–36} or extrinsic magnetism caused by magnetic doping^{37–40}, magnetic field^{41,42} and magnetic proximity effect^{43–46}, while the latter is related to the chemical compositions. The past years have seen impressive progress for identifying such AVH effect in single-layer materials^{29–46}. In all the prior studies, there is one default assumption, namely, the magnetism must be ferromagnetic. Compared with ferromagnetism, antiferromagnetic materials have great potential in the next generation of valleytronic and spintronic applications thanks to the intrinsic advantages such as robustness against magnetic field perturbation, ultrafast dynamics, stray field-free operation^{47,48}. However, to our knowledge, it is still unclear how to realize stable AVH effect in single-layer materials with an antiferromagnetic order.

In the present work, we show by model analysis that the realization of stable AVH effect can be extended to single-layer materials with an antiferromagnetic order. The proposed general

design principle for this extension correlates with the introduction of nonuniform potentials to break the PT symmetry [invariance under the combined operation of spatial inversion (P) and time reversal (T)]. Based on first-principles calculations, we further demonstrate this design principle by stacking antiferromagnetic monolayer MnPSe_3 on ferroelectric monolayer Sc_2CO_2 and realize the AVH effect. Such AVH effect is shown to exhibit a tantalizing stacking pattern depended character. Moreover, we reveal that the AVH effect in monolayer MnPSe_3 can be switched on or off by reversing the ferroelectric polarization of monolayer Sc_2CO_2 . This extension of AVH effect to single-layer materials with an antiferromagnetic order is of great significance from both fundamental perspective and for potential use in devices.

RESULTS AND DISCUSSION

Introducing nonuniform potentials to break PT symmetry

Our proposed design principle for realizing AVH effect in single-layer materials with an antiferromagnetic order is schematically illustrated in Fig. 1. Without losing the generality, we take monolayer MnPSe_3 as an example to discuss the scheme by considering the fact that monolayer MnPSe_3 is known as a typical Néel antiferromagnetic semiconductor with spontaneous valley polarization. Monolayer MnPSe_3 exhibits a hexagonal lattice with the space group of D_{3d} (see Supplementary Fig. 1a). Without considering exchange interaction, its structure hosts the inversion symmetry P . In monolayer MnPSe_3 , the Mn atoms constitute two sublattices, which are referred to as A and B sublattices. Although the A and B sublattices are structurally equivalent, their spin orientations are opposite. In this regard, neither inversion symmetry (P) nor time-reversal symmetry (T) is preserved. However, it shows invariance under the simultaneous time reversal and spatial inversion, namely, PT symmetry. Because of the PT symmetry, the spin and valley polarization occur spontaneously in such antiferromagnetic monolayers, as schematically shown in Fig. 1a. Also protected by the PT symmetry, the valley spin splitting is prohibited, yielding the spin degeneracy for the K and K' valleys. Such spin degeneracy in antiferromagnetic monolayers forbids the realization of AVH effect. For example, upon shifting Fermi level between the K and K' valleys in the

¹School of Physics, State Key Laboratory of Crystal Materials, Shandong University, Shandan Str. 27, Jinan 250100, China. ✉email: daiy60@sina.com; yandong.ma@sdu.edu.cn

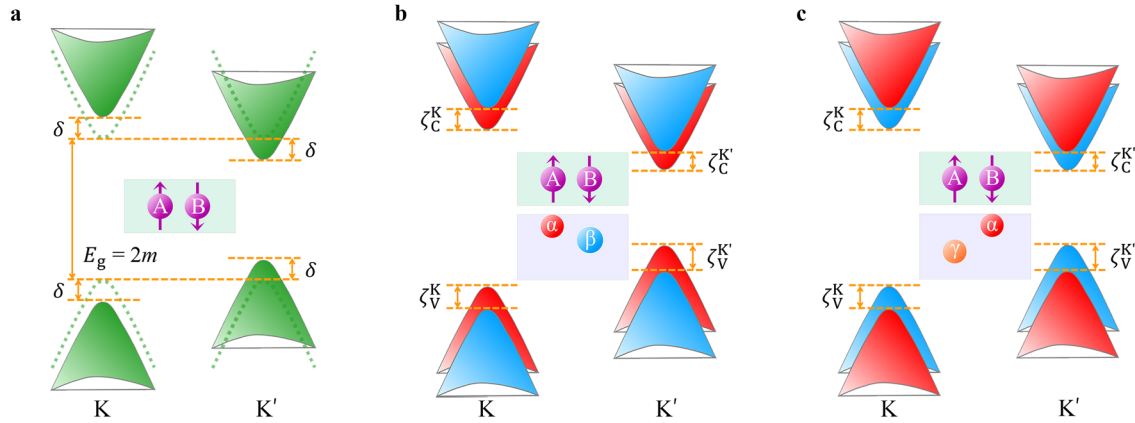


Fig. 1 Schematic band structures of monolayer MnPSe₃. Schematic diagrams for the K and K' valleys of monolayer MnPSe₃ **a** without and **b**, **c** with nonuniform potentials on the A and B sublattices. Dotted and solid cones in **a** represent the valleys without and with considering SOC, respectively. Red and blue cones in **b** and **c** correspond to two spin states, respectively.

conduction bands, the spin-up and spin-down electrons from the K' valley would accumulate at opposite edges of the sample in the presence of an in-plane electric field, preventing the AVH effect.

If we introduce nonuniform potentials to neighboring Mn atoms, the equivalence of the A and B sublattices is deformed, which will break the *PT* symmetry. Without the protection of *PT* symmetry, the valley spin splitting at the K and K' valleys would be achieved (see Fig. 1b), rendering the observation of AVH effect. Such valley spin splitting is different from the case in nonmagnetic materials, where the valley spin splitting relates to Zeeman splitting^{14,15,49}. To preserve the valley physics, the nonuniform potentials introduced here should be regular. More importantly, it is natural to expect that the spin orders at both the K and K' valleys can be reversed by reversing the nonuniform potentials introduced to A and B sublattices (Fig. 1c), which would enrich the AVH effect in antiferromagnetic monolayers.

Given the proposed design principle, we construct a **k**-**p** model to verify it. The spin-full Hamiltonian with excluding SOC for low-energy quasiparticles near the K(K') valley of a honeycomb lattice can be expressed as¹⁶

$$H^0 = v_F s_0 (\tau_z \sigma_x p_x + \tau_0 \sigma_y p_y) + m s_z \tau_0 \sigma_z \quad (1)$$

Here, p and v_F represent the momentum operator and the massless Fermi velocity, respectively. τ_α , σ_α , and s_α ($\alpha = x, y, z, 0$) are the Pauli matrices for the valley, isospin, and spin degree of freedom, respectively. The mass term (m), referring to an AFM perturbation, creates a band gap of $E_g = 2m$ for both spins, preserving the spin and energy degeneracy. When taking SOC into account, the Hamiltonian for SOC is introduced as

$$H^{\text{SOC}} = \delta s_z \tau_z \sigma_z \quad (2)$$

where δ is the SOC parameter. In the presence of SOC, the band gap is enlarged by 2δ at the K valley and reduced by 2δ at the K' valley. As a result, the energetic degeneracy of the K and K' valleys are lifted, but the spin degeneracy is preserved due to the invariance of the $H^0 + H^{\text{SOC}}$ under simultaneous time reversal and spatial inversion. The term for the nonuniform potential between two sublattices can be written as:

$$H_{\text{ex}} = \frac{\zeta}{2} s_0 \tau_0 \sigma_z \quad (3)$$

where $\frac{\zeta}{2}$ represents the strength of the nonuniform potential. In this case, the $H^0 + H^{\text{SOC}} + H_{\text{ex}}$ would not be invariance under simultaneous time reversal and spatial inversion. This drives the bands from one sublattice to shift upward with respect to those from the other, resulting in a valley spin splitting of ζ at the K and K' valleys. According to the total Hamiltonian $H = H^0 + H^{\text{SOC}} + H_{\text{ex}}$, the eigenvalues of the highest valence

bands are estimated to be $(-m - \delta - \frac{\zeta}{2})$ and $(-m - \delta + \frac{\zeta}{2})$ for spin-up and spin-down at the K valley, respectively, and $(-m + \delta - \frac{\zeta}{2})$ and $(-m + \delta + \frac{\zeta}{2})$ for spin-up and spin-down at K' valley. And the eigenvalues of the lowest conduction bands are found to be $(m + \delta + \frac{\zeta}{2})$ and $(m + \delta - \frac{\zeta}{2})$ for spin-up and spin-down at the K valley, respectively, and $(m - \delta + \frac{\zeta}{2})$ and $(m - \delta - \frac{\zeta}{2})$ for spin-up and spin-down at K' valley. When reversing the nonuniform potential between two sublattices, the sign of H_{ex} is reversed, leading to the opposite valley spin splitting at the K and K' valleys. These results firmly indicate that the proposed design principle for realizing AVH effect in antiferromagnetic monolayers is feasible physically.

Stacking-dependent AVH effect in MnPSe₃/Sc₂CO₂

Having established the feasibility of the proposed design principle, next we discuss its realization in real materials. The proximity effect is proposed here to introduce nonuniform potentials on the A and B sites regularly. For detail, we consider monolayer Sc₂CO₂ as the substrate to induce the proximity effect in monolayer MnPSe₃. The crystal structure of monolayer Sc₂CO₂ is shown in Supplementary Fig. 1b. It exhibits a hexagonal lattice with the space group P3m1. Due to the asymmetric displacement of inner C atomic layer with respect to Sc atomic layers, it hosts intrinsic ferroelectricity with out-of-plane polarization⁵⁰. The band structure shown in Supplementary Fig. 1d suggests that monolayer Sc₂CO₂ is a semiconductor with an indirect band gap of 1.79 eV. Concerning the stacking between monolayer MnPSe₃ and Sc₂CO₂, a 2×2 supercell of Sc₂CO₂ is adopted to match the unit cell of MnPSe₃. This results in a compressive strain of about 6% for Sc₂CO₂ layer, which is in an accessible range in experiments^{51,52}. It should be noted that when two van der Waals (vdW) materials are brought into contact, the lattice would undergo relaxation, while could result in lattice reconstructions as well as strain⁵³. To reveal strain effect on AVH physics, we also investigate the band structures of MnPSe₃/Sc₂CO₂ under different tensile strain, and similar results are obtained (see Supplementary Fig. 2). According to the previous works^{46,54–56}, three typical stacking patterns (i.e., h-I₁, h-II₁ and h-III₁, as shown in Fig. 2a) with the polarization of Sc₂CO₂ pointing away from the interface are considered for the stacking between monolayer MnPSe₃ and Sc₂CO₂. These three patterns can induce three distinct proximity effects on MnPSe₃. In h-I₁ pattern, the Mn₁ atoms sit above the top-O sites of Sc₂CO₂, and the Mn₂ atoms are right above the Sc atoms in the second layer of Sc₂CO₂. In h-II₁ pattern, the Mn₁ atoms lie above the C atoms in the middle layer, and the Mn₂ atoms are right above the top-O atoms. In h-III₁ pattern, the Mn₁ atoms sit above the Sc atoms in the second layer, and Mn₂ atoms

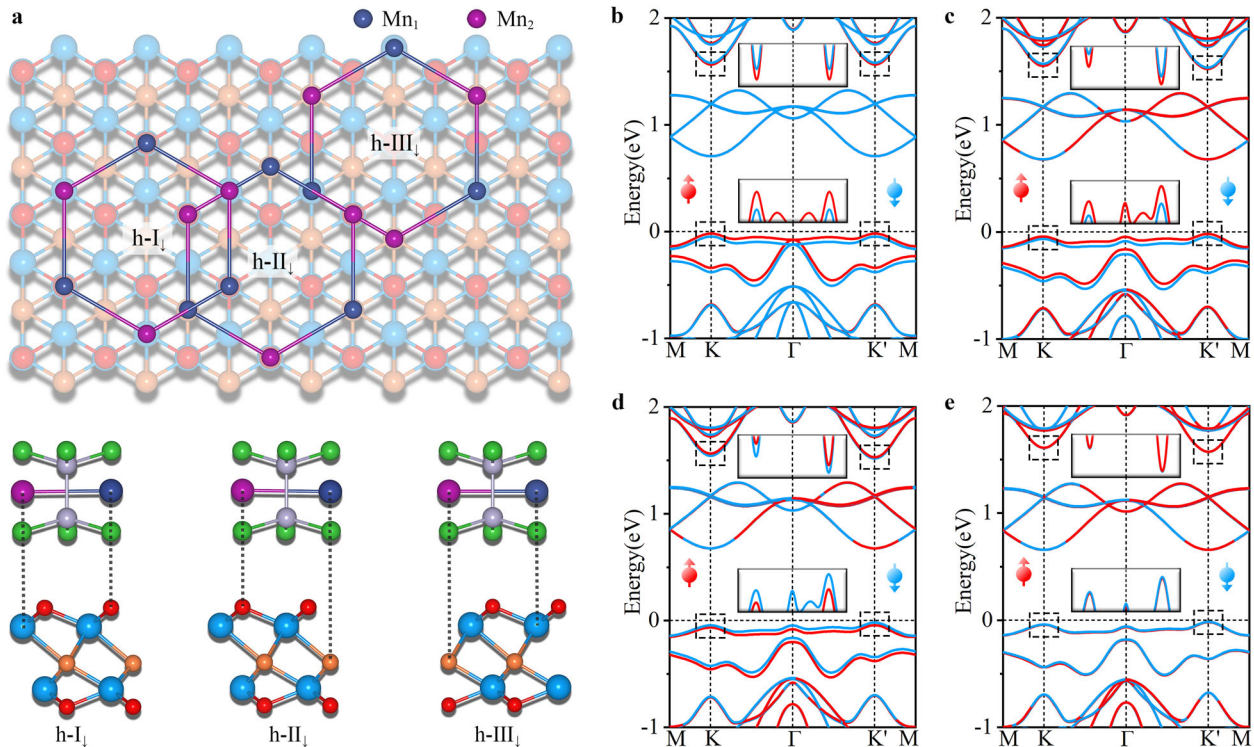


Fig. 2 **Structural configurations and band structures.** **a** Crystal structures of $h-I_1$, $h-II_1$ and $h-III_1$. Band structures of $h-I_1$ **b** without and **c** with considering SOC. **d** Band structure of $h-II_1$ with considering SOC. **e** Band structure of $h-III_1$ with considering SOC. Blue and red lines in **b–e** correspond to spin-down and spin-up states, respectively. The Fermi level is set to 0 eV.

lie above the C atom in the middle layer of Sc_2CO_2 . Concerning other stacking patterns, the proximity effect is expected to be similar to or in between the cases of $h-I_1/II_1/III_1$ configurations. Taking the configuration with Mn atom sitting above the center of Sc-O-C triangle as an example, we calculate its band structure. As shown in Supplementary Fig. 3, the scenario is similar to that of $h-III_1$ configuration.

In $h-I_1$ configuration, the Mn_1 atoms would experience an extra interaction due to their proximity to the top-O sites of Sc_2CO_2 , while the Mn_2 atoms would endure with a relatively small interaction as they lie farther. This can be described by the scenario illustrated in Fig. 1b, which introduces nonuniform potentials into the two sublattices of Mn atoms. The band structure of $h-I_1$ configuration without considering SOC is shown in Fig. 2b and Supplementary Fig. 4a. The conduction band minimum (CBM) and valence band maximum (VBM) are contributed by monolayer Sc_2CO_2 and $MnPSe_3$, respectively, forming a type-II band alignment. The degenerate valleys of $MnPSe_3$ in both the conduction and valence bands locating at the K and K' points are preserved after stacking on Sc_2CO_2 . However, as shown in Fig. 2b, the interesting valley spin splitting occurs in both the bottom conduction and top valence bands of $MnPSe_3$ at the K/K' point, which correlates to the nonuniform potentials induced by stacking. Although the valleys of $MnPSe_3$ in the conduction bands submerge in the bands of Sc_2CO_2 , they are still investigated for comparison. The valley spin splitting in the valence bands ($\zeta_V^K = \zeta_V^{K'}$) and conduction bands ($\zeta_C^K = \zeta_C^{K'}$) are estimated to be 28.5 and 16.7 meV, respectively. Such sizeable valley spin splitting stands in sharp contrast to the valley spin splitting in nonmagnetic materials which are induced by SOC and P breaking.

When taking SOC into account, as shown in Fig. 2c, the character of valley spin splitting of $MnPSe_3$ is maintained at both the K and K' valleys, but the values of valley spin splitting at K and K' valleys are no longer equal; see Supplementary Table 1. In this case, the energetic degeneracy of the K and K' valleys in $MnPSe_3$ is

lifted, leading to the spontaneous valley polarization. Particularly, the valley polarization in the valence band is as large as 24.6 meV. The coexistence of valley spin splitting and valley polarization would ensure the observation of AVH effect in antiferromagnetic monolayer of $MnPSe_3$, as we will show later.

As discussed above, the valley spin splitting relates to the nonuniform potentials induced by the proximity effect. Therefore, by engineering the stacking pattern, the valley spin splitting can be modulated. In $h-II_1$ configuration, the Mn_2 atoms experience an extra interaction due to their proximity to the top-O sites of Sc_2CO_2 , while the Mn_1 atoms endure with a relatively small interaction as they lie farther. This corresponds to the scenario illustrated in Fig. 1c. Accordingly, the nonuniform potentials introduced to Mn_1 and Mn_2 atoms in $h-II_1$ configuration is reversed with respect to those in $h-I_1$ configuration. The band structure of $h-II_1$ configuration with considering SOC is presented in Fig. 2d. It shares similar features to the band structure of $h-I_1$. The interesting valley spin splitting and spontaneous valley polarization are observed at the K and K' valleys of $MnPSe_3$, and the magnitudes are comparable to that in $h-I_1$ configurations. However, the sign of the valley spin splitting is opposite to that of $h-I_1$ configurations, which is consistent with the proposed design principle. Such simultaneous existence of valley spin splitting and valley polarization would facilitate the AVH effect as well.

Different from the cases of $h-I_1$ and $h-II_1$ configurations, both the Mn_1 and Mn_2 atoms in $h-III_1$ configuration experience a weak extra interaction since they lie far away from the atoms of Sc_2CO_2 . Thus, the nonuniform potentials introduced to Mn_1 and Mn_2 atoms by the proximity effect would be rather weak. According to the proposed design principle, the valley spin splitting of $MnPSe_3$ in $h-III_1$ configuration would be tiny. The band structure of $h-III_1$ configuration with considering SOC is displayed in Fig. 2e. As expected, the valley spin splitting is as small as 2.3 meV (2.6 meV) at the K (K') valley in the valence band, while it is even 1 meV (1 meV) in the conduction band of $MnPSe_3$, although large

spontaneous valley polarization is preserved. In this case, the observation of AVH effect in h-III_↓ configuration is difficult to achieve. Therefore, the valley spin splitting in MnPSe₃ is indeed stacking dependent and thus can be engineered by modulating the stacking pattern, while holds great promise for practical applications. There are two points we wish to stress. First, currently, the stacking orders of 2D vdW materials can be well modulated in experiments^{57,58}. Second, although the three stacking patterns might coexist in macroscopic area, the different configurations would be well-separated and the domains for them would be well-defined^{59,60}.

The nonuniform potentials introduced to Mn₁ and Mn₂ atoms by the proximity effect for all these three stacking patterns can also be straightforwardly reflected by the variation of magnetic moments. For freestanding MnPSe₃, the magnetic moments on Mn₁ and Mn₂ atoms are found to be 4.52 and −4.52 μ_B, respectively, which is protected by the *PT* symmetry. When stacking MnPSe₃ on Sc₂CO₂ to form the h-I_↓ configuration, the magnetic moment on Mn₁ atom changes to 4.508 μ_B, while the magnetic moment on Mn₂ atom experiences with a relatively slight change (−4.513 μ_B). This suggests the nonuniform potentials on the Mn₁ and Mn₂ atoms. As compared with h-I_↓ configuration, the absolute values of the magnetic moments on Mn₁ and Mn₂ atoms in h-II_↓ configuration are exchanged, but the signs of the magnetic moments remain the same. Namely, the magnetic moments on Mn₁ and Mn₂ atoms in h-II_↓ configuration are found to be 4.513 and −4.508 μ_B, respectively. This can be easily understood by recalling the reversal of the atomic environments for Mn₁ and Mn₂ atoms in h-I_↓ and h-II_↓ configurations. For h-III_↓ configuration, the magnetic moments on Mn₁ and Mn₂ atoms slightly change to 4.514 and −4.514 μ_B, respectively. The preservation of identical absolute values of the magnetic moments on Mn₁ and Mn₂ atoms in h-III_↓ configuration relates to the weak extra interactions on both Mn atoms.

In 2D hexagonal lattices with inversion symmetry breaking, the K and K' valleys will exhibit a nonzero Berry curvature along the out-of-plane direction. The Berry curvature is defined as⁶¹

$$\Omega(\mathbf{k}) = - \sum_n \sum_{n' \neq n} f_n \frac{2Im \langle \psi_{n\mathbf{k}} | v_x | \psi_{n'\mathbf{k}} \rangle \langle \psi_{n'\mathbf{k}} | v_y | \psi_{n\mathbf{k}} \rangle}{(E_n - E_{n'})^2} \quad (4)$$

Here, f_n is the Fermi-Dirac distribution function, $\psi_{n\mathbf{k}}$ is the Bloch wave function with eigenvalue E_n , and v_x/v_y is the velocity operator along x/y direction. The calculated Berry curvatures of the spin-up and spin-down channels over the 2D Brillouin zone for monolayer MnPSe₃ are shown in Fig. 3a. Obviously, the Berry curvatures for the same spin state around the K and K' valleys are opposite, and the Berry curvatures for spin-up and spin-down states at the same valley are opposite as well. Note that under a longitudinal in-plane electric field, the Bloch carriers will acquire an anomalous transverse velocity proportional to the Berry curvature: $v_a \sim E \times \Omega(\mathbf{k})$. In monolayer MnPSe₃, when shifting the Fermi level between the K and K' valleys in the valence band, protected by the *PT* symmetry, the spin-down and spin-up holes from the K' valley will gather to opposite edges of the sample in the presence of an in-plane electric field, see Fig. 3b. In this regard, a net spin current is generated, which results in the spin Hall effect, however, the AVH effect is absent. In h-I_↓ configuration, because of the additional valley spin splitting, the spin degeneracy is lifted. When shifting the Fermi level between the K and K' valleys in the valence band, only the spin-down holes from the K' valley move to the bottom boundary of the sample under an in-plane electric field; see Fig. 3c. This gives rise to the long sought AVH effect in antiferromagnetic monolayers. In addition, the accumulated spin-down holes will result in a net charge/spin current. Similar to the case of h-I_↓ configuration, when shifting the Fermi level between the K and K' valleys in the valence band of the h-II_↓ configuration, the spin-up holes from the K' valley will

accumulate at the top edge of the sample (Fig. 3d), which results into the AVH effect as well.

Ferroelectrically controllable AVH effect

Note that monolayer Sc₂CO₂ is a 2D ferroelectric crystal with an out-of-plane polarization, its polarization direction can be reversed under a short-term out-of-plane electric field. Note that the reversed polarized state will be retained when the external electric field is removed. Such ferroelectric switching might affect the electronic properties of the MnPSe₃/Sc₂CO₂. In the following, we investigate the properties of the three typical stacking patterns with switching the ferroelectric polarization of Sc₂CO₂ from downward to upward, which are referred to as h-I_↑, h-II_↑, h-III_↑, respectively; see Supplementary Fig. 5. Figure 4a presents the band structures of h-I_↑, h-II_↑ and h-III_↑ configurations with considering SOC. The band structures of all these three configurations share similar characters. In all these three configurations, the Fermi level crosses the bottom of the conduction band and top of the valence band, yielding a metallic nature. More interestingly, the valleys of MnPSe₃ in both the conduction and valence bands are submerged in the trivial bands of Sc₂CO₂, restricting any potential utilization of these valleys. In other word, under the ferroelectric switching, all these three configurations undergo a semiconductor-to-metal transition. Such transition is also accompanied with the disappearance of valley physics as well as the AVH effect. Accordingly, the AVH effect in h-I_↓ and h-II_↓ configurations is ferroelectrically controllable, benefiting for developing controllable valleytronic devices.

To understand the underlying mechanism of the ferroelectric-polarization-dependent properties, we calculate the plane-average electrostatic potentials of monolayer MnPSe₃, monolayer Sc₂CO₂, h-I_↓ and h-I_↑ (Fig. 4b and Supplementary Fig. 6). It can be seen that arising from the asymmetric structure, intrinsic polarization occurs along the out-of-plane direction, leading to the different work functions at the two sides of monolayer Sc₂CO₂. Accordingly, upon contacting monolayer MnPSe₃ with Sc₂CO₂ in different polarized states, the distinctly different band alignments forms, as shown in Fig. 4c. When the polarization of monolayer Sc₂CO₂ points away from the interface, the CBM of Sc₂CO₂ locates above the VBM of MnPSe₃, inhibiting the transfer of electrons between Sc₂CO₂ and MnPSe₃. The valley feature in the valence band from MnPSe₃ is preserved. In contrast, when the polarization pointing to the interface, the CBM of MnPSe₃ shifts below the VBM of Sc₂CO₂, prompting the electron transfer from Sc₂CO₂ to MnPSe₃, leading to the metallic nature. By comparing Supplementary Figs. 1c, d and 4, it can be seen that the bands from the constituent layers are roughly similar to the corresponding free-standing ones, which indicates the weak hybridization between them for both the upward-polarization and down-polarization cases. The polarization reversal only changes the band alignment and gives rise to different band contributions around the Fermi level, leading to the submersion of valleys in the trivial bands or not. The charge transfer character between Sc₂CO₂ to MnPSe₃ in h-I_↑, h-II_↑ and h-III_↑ configurations is also confirmed by the charge density differences shown in Supplementary Fig. 7. While for h-I_↓, h-II_↓ and h-III_↓ configurations, the charge redistribution occurs around the interface. The charge transfer caused by polarization reversal could lead to semiconductor-to-metal transition. Such transition is accompanied with the submersion of valleys in the trivial bands and thus deforms the valley physics. While for the case under hole doping, it will not lead to the submersion of valleys in the trivial bands, which could preserve the valley physics. With these results in hand, we can understand the polarization dependent behaviors in MnPSe₃/Sc₂CO₂.

To summarize, through model analysis, a general design principle for realizing stable AVH effect in antiferromagnetic monolayers is proposed, which involves the introduction of nonuniform potentials to Mn₁ and Mn₂ atoms to break the *PT* symmetry. Using

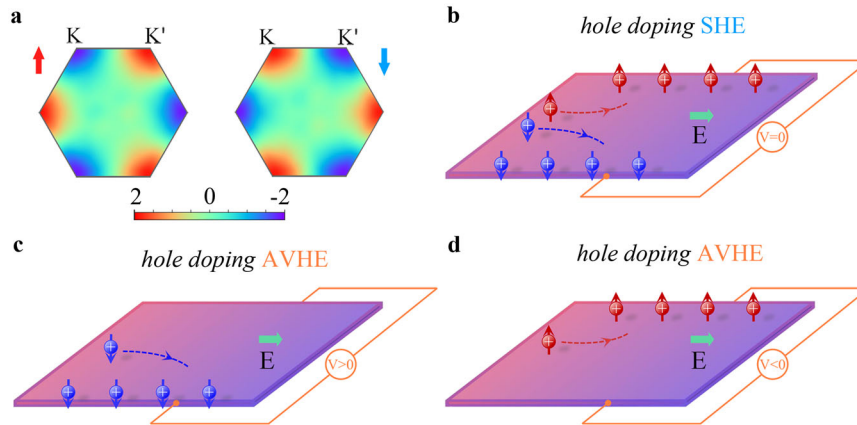


Fig. 3 Berry curvatures and AVH effect. **a** Berry curvatures of the spin-up and spin-down channels over the 2D Brillouin zone for monolayer MnPSe_3 . **b** Diagram of the spin and valley Hall effects in monolayer MnPSe_3 under hole doping in presence of an in-plane electric field. Diagrams of the spin Hall and AVH effects in **c** $h\text{-I}_1$ and **d** $h\text{-II}_1$ configurations under hole doping in presence of an in-plane electric field. Red/blue arrows in **b–d** indicate spin-up/down states, and the “+”/“–” symbols indicate holes/electrons from the K' valley.

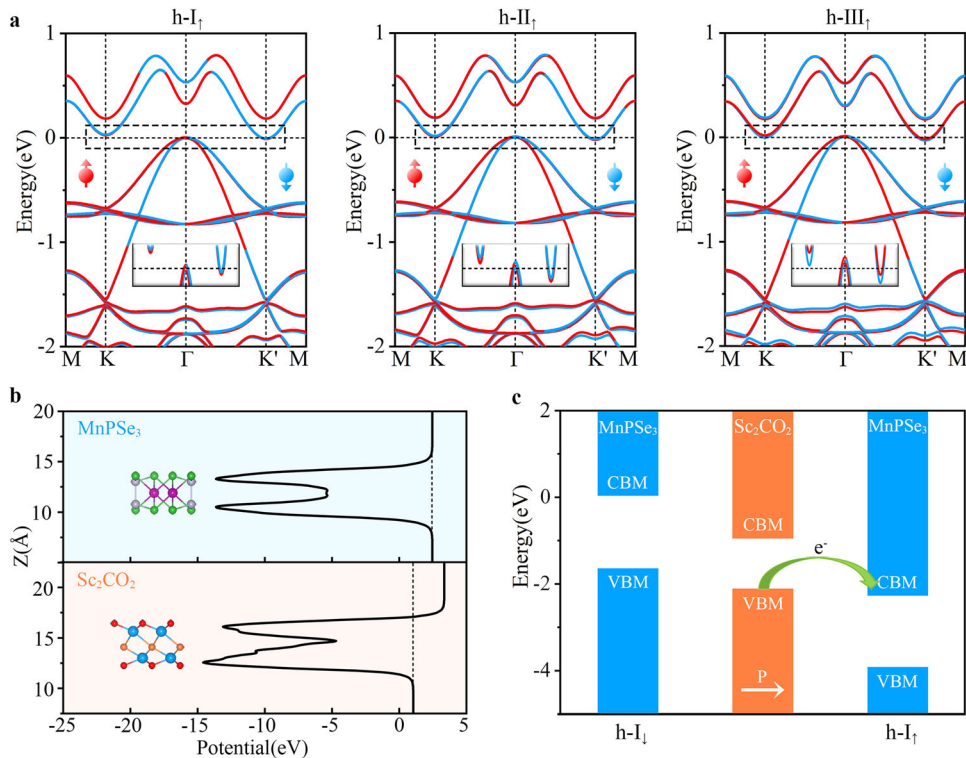


Fig. 4 Ferroelectric-polarization-dependent properties in $\text{MnPSe}_3/\text{Sc}_2\text{CO}_2$. **a** Band structures of $h\text{-I}_1$, $h\text{-II}_1$ and $h\text{-III}_1$ with considering SOC. Blue and red lines in **a** correspond to spin-down and spin-up states, respectively. The Fermi level is set to 0 eV. **b** Plane-averaged electrostatic potentials of monolayer MnPSe_3 and Sc_2CO_2 along the z direction. **c** Band alignments of $h\text{-I}_1$ and $h\text{-II}_1$ with respect to the vacuum level.

first-principles calculations, the proposed design principle is further demonstrated by stacking antiferromagnetic monolayer MnPSe_3 on ferroelectric monolayer Sc_2CO_2 . The realized AVH effect hosts the stacking pattern depended character. In addition, the AVH effect in $\text{MnPSe}_3/\text{Sc}_2\text{CO}_2$ can be switched on or off under ferroelectric switching of monolayer Sc_2CO_2 .

METHODS

Density functional theory calculations

Our first-principles calculations are performed based on density functional theory (DFT) methods as implemented in the Vienna ab initio simulation

package (VASP)^{62,63}. The generalized gradient approximation (GGA) in form of Perdew-Burke-Ernzerhof (PBE) functional is used to describe the exchange-correlation interaction⁶⁴. The cutoff energy is set to 500 eV. Crystal structures are fully relaxed with the convergence criteria of 10^{-5} eV and $0.01 \text{ eV}\text{\AA}^{-1}$ for energy and force, respectively. The Brillouin zone is sampled with Monkhorst-Pack grids of $9 \times 9 \times 1$. To avoid interactions between adjacent periodical structures, the vacuum space along the z direction is set to 30 Å. The zero damping DFT-D3 method is utilized to treat the vdW interaction⁶⁵. To describe the strong correlation effects, the effective on-site Hubbard term of $U = 4 \text{ eV}$ is set for the 3d electrons of the Mn atom, as this value is employed in previous works^{44,66,67}. Berry curvature is calculated using the maximally localized Wannier function method as implemented in the WANNIER90 package⁶⁸.

DATA AVAILABILITY

The authors declare that the data supporting the findings of this study are available within the paper and its supplementary information files.

CODE AVAILABILITY

The central codes used in this paper are VASP and WANNIER90. Detailed information related to the license and user guide are available at <http://www.wannier.org> and <https://www.vasp.at>.

Received: 1 September 2021; Accepted: 20 January 2022;

Published online: 25 February 2022

REFERENCES

- Xiao, D., Yao, W. & Niu, Q. Valley-contrasting physics in graphene: magnetic moment and topological transport. *Phys. Rev. Lett.* **99**, 236809 (2007).
- Yao, W., Xiao, D. & Niu, Q. Valley-dependent optoelectronics from inversion symmetry breaking. *Phys. Rev. B* **77**, 235406 (2008).
- Berkelbach, T., Hybertsen, M. & Reichman, D. Theory of neutral and charged excitons in monolayer transition metal dichalcogenides. *Phys. Rev. B* **88**, 045318 (2013).
- Lu, H., Yao, W., Xiao, D. & Shen, S. Intervalley scattering and localization behaviors of spin-valley coupled dirac fermions. *Phys. Rev. Lett.* **110**, 016806 (2013).
- Sanchez, O., Ovchinnikov, D., Misra, S., Allain, A. & Kis, A. Valley polarization by spin injection in a light-emitting van der Waals heterojunction. *Nano Lett.* **16**, 5792 (2016).
- Schaibley, J. R. et al. Valleytronics in 2D materials. *Nat. Rev. Mater.* **1**, 16055 (2016).
- Vitale, S. A. et al. Valleytronics: opportunities, challenges, and paths forward. *Small* **14**, 1801483 (2018).
- Sham, L. J., Allen, S. J. Jr., Kamgar, A. & Tsui, D. C. Valley-valley splitting in inversion layers on a high-index surface of silicon. *Phys. Rev. Lett.* **40**, 472 (1978).
- Ohkawa, F. J. & Uemura, Y. Theory of valley splitting in an N-channel (100) inversion layer of Si. Formulation by extended zone effective mass theory. *J. Phys. Soc. Jpn* **43**, 907 (1977).
- Rycerz, A., Tworzydło, J. & Beenakker, C. W. J. Valley filter and valley valve in graphene. *Nat. Phys.* **3**, 172 (2007).
- Akhmerov, A. R. & Beenakker, C. W. J. Detection of valley polarization in graphene by a superconducting contact. *Phys. Rev. Lett.* **98**, 157003 (2007).
- Wu, S. et al. Electrical tuning of valley magnetic moment through symmetry control in bilayer MoS₂. *Nat. Phys.* **9**, 149 (2013).
- Sie, E. J. et al. Valley-selective optical Stark effect in monolayer WS₂. *Nat. Mater.* **14**, 290 (2015).
- Zhu, Z. Y., Cheng, Y. C. & Schwingenschlög, U. Giant spin-orbit-induced spin splitting in two-dimensional transition-metal dichalcogenide semiconductors. *Phys. Rev. B* **84**, 153402 (2011).
- Xiao, D., Liu, G.-B., Feng, W., Xu, X. & Yao, W. Coupled spin and valley physics in monolayers of MoS₂ and other Group-VI dichalcogenides. *Phys. Rev. Lett.* **108**, 196802 (2012).
- Li, X., Cao, T., Niu, Q., Shi, J. & Feng, J. Coupling the valley degree of freedom to antiferromagnetic order. *Proc. Natl Acad. Sci. USA* **110**, 3738 (2013).
- Tong, W.-Y. & Duan, C.-G. Electrical control of the anomalous valley Hall effect in antiferrovalley bilayers. *npj Quant. Mater.* **2**, 47 (2017).
- Xu, L. et al. Large valley splitting in monolayer WS₂ by proximity coupling to an insulating antiferromagnetic substrate. *Phys. Rev. B* **97**, 041405 (2018).
- Ma, Y. et al. Conduction-band valley spin splitting in single-layer H-Ti₂O. *Phys. Rev. B* **97**, 035444 (2018).
- Ke, C. et al. Large and controllable spin-valley splitting in two-dimensional WS₂/h-VN heterostructure. *Phys. Rev. B* **100**, 195435 (2019).
- Hu, H., Tong, W.-Y., Shen, Y.-H. & Duan, C.-G. Electrical control of the valley degree of freedom in 2D ferroelectric/antiferromagnetic heterostructures. *J. Mater. Chem. C* **8**, 8098 (2020).
- Ma, X. et al. Tunable valley splitting and anomalous valley Hall effect in VTe₂/Ga₂S₃ heterostructures. *J. Mater. Chem. C* **8**, 14895 (2020).
- Li, S. et al. Valley-dependent properties of monolayer MoSi₂N₄, WSi₂N₄, and MoSi₂As₄. *Phys. Rev. B* **102**, 235435 (2020).
- Yang, C., Song, Z., Sun, X. & Lu, J. Valley pseudospin in monolayer MoSi₂N₄ and MoSi₂As₄. *Phys. Rev. B* **103**, 035308 (2021).
- Dou, K. et al. Promising valleytronic materials with strong spin-valley coupling in two-dimensional MN₂X₂ (M = Mo, W; X = F, H). *Appl. Phys. Lett.* **117**, 172405 (2020).
- Lei, C. et al. Nonvolatile controlling valleytronics by ferroelectricity in 2H-VSe₂/Sc₂CO₂ van der Waals heterostructure. *J. Phys. Chem. C* **125**, 2802 (2021).
- Mak, K. F., He, K., Shan, J. & Heinz, T. F. Control of valley polarization in monolayer MoS₂ by optical helicity. *Nat. Nanotech.* **7**, 494 (2012).
- Zeng, H., Dai, J., Yao, W., Xiao, D. & Cui, X. Valley polarization in MoS₂ monolayers by optical pumping. *Nat. Nanotech.* **7**, 490 (2012).
- Tong, W.-Y., Gong, S.-J., Wan, X. & Duan, C.-G. Concepts of ferrovalley material and anomalous valley Hall effect. *Nat. Commun.* **7**, 13612 (2016).
- Liu, J. et al. Intrinsic valley polarization of magnetic VSe₂ monolayers. *J. Phys. Condens. Matter* **29**, 255501 (2017).
- Zhao, P. et al. Single-layer LaBr₂: two-dimensional valleytronic semiconductor with spontaneous spin and valley polarizations. *Appl. Phys. Lett.* **115**, 261605 (2019).
- Song, Z. et al. Spontaneous valley splitting and valley pseudospin field effect transistors of monolayer VAgP₂Se₆. *Nanoscale* **10**, 13986 (2018).
- Peng, R. et al. Intrinsic anomalous valley Hall effect in single-layer Nb₃I₈. *Phys. Rev. B* **102**, 035412 (2020).
- Du, W. et al. Prediction of single-layer TiVl₆ as a promising two-dimensional valleytronic semiconductor with spontaneous valley polarization. *J. Mater. Chem. C* **8**, 13220 (2020).
- Zang, Y. et al. Large valley-polarized state in single-layer NbX₂ (X = S, Se): theoretical prediction. *Nano Res.* **14**, 834 (2021).
- Cheng, H.-X., Zhou, J., Ji, W., Zhang, Y.-N. & Feng, Y.-P. Two-dimensional intrinsic ferrovalley GdI₂ with large valley polarization. *Phys. Rev. B* **103**, 125121 (2021).
- Peng, R., Ma, Y., Zhang, S., Huang, B. & Dai, Y. Valley polarization in Janus single-layer MoSSe via magnetic doping. *J. Phys. Chem. Lett.* **9**, 3612 (2018).
- Xu, X. et al. Nonmetal-atom-doping-induced valley polarization in single-layer Ti₂O. *J. Phys. Chem. Lett.* **10**, 4535 (2019).
- Zhang, T. et al. Two-dimensional valleytronics in single-layer t-ZrNY (Y = Cl, Br) predicted from first principles. *J. Phys. Chem. C* **124**, 20598 (2020).
- Lei, C. et al. Valley polarization in monolayer CrX₂ (X = S, Se) with magnetically doping and proximity coupling. *N. J. Phys.* **22**, 033002 (2020).
- Aivazian, G. et al. Magnetic control of valley pseudospin in monolayer WSe₂. *Nat. Phys.* **11**, 148 (2015).
- Zhang, X.-X. et al. Magnetic brightening and control of dark excitons in monolayer WSe₂. *Nat. Nanotech.* **12**, 883 (2017).
- Qi, J., Li, X., Niu, Q. & Feng, J. Giant and tunable valley degeneracy splitting in MoTe₂. *Phys. Rev. B* **92**, 121403 (2015).
- Zhou, B., Li, Z., Wang, J., Niu, X. & Luan, C. Tunable valley splitting and an anomalous valley Hall effect in hole-doped WS₂ by proximity coupling with a ferromagnetic MnO₂ monolayer. *Nanoscale* **11**, 13567 (2019).
- Pei, Q., Zhou, B., Mi, W. & Cheng, Y. Triferroic material and electrical control of valley degree of freedom. *ACS Appl. Mater. Interfaces* **11**, 12675 (2019).
- Zhang, Z., Ni, X., Huang, H., Hu, L. & Liu, F. Valley splitting in the van der Waals heterostructure WSe₂/CrI₃: the role of atom superposition. *Phys. Rev. B* **99**, 115441 (2019).
- Jungwirth, T. et al. The multiple directions of antiferromagnetic spintronics. *Nat. Phys.* **14**, 200 (2018).
- Baltz, V. et al. Antiferromagnetic spintronics. *Rev. Mod. Phys.* **90**, 015005 (2018).
- Liu, G.-B., Shan, W.-Y., Yao, Y., Yao, W. & Xiao, D. Three-band tight-binding model for monolayers of group-VIB transition metal dichalcogenides. *Phys. Rev. B* **88**, 085433 (2013).
- Chandrasekaran, A., Mishra, A. & Singh, A. K. Ferroelectricity, antiferroelectricity, and ultrathin 2D electron/hole gas in multifunctional monolayer MXene. *Nano Lett.* **17**, 3290 (2017).
- Lee, C., Wei, X. D., Kysar, J. W. & Hone, J. Measurement of the elastic properties and intrinsic strength of monolayer graphene. *Science* **321**, 385 (2008).
- Castellanos-Gomez, A. et al. Mechanical properties of freely suspended semiconducting graphene-like layers based on MoS₂. *Nanoscale Res Lett.* **7**, 233 (2012).
- Halbertal, D. et al. Moiré metrology of energy landscapes in van der Waals heterostructures. *Nat. Commun.* **12**, 242 (2021).
- Li, L. & Wu, M. Binary compound bilayer and multilayer with vertical polarizations: two-dimensional ferroelectrics, multiferroics, and nanogenerators. *ACS Nano* **11**, 6382 (2017).
- Liang, Y., Shen, S., Huang, B., Dai, Y. & Ma, Y. Intercorrelated ferroelectrics in 2D van der Waals materials. *Mater. Horiz.* **8**, 1683 (2021).
- He, J., Li, S., Bandyopadhyay, A. & Frauenheim, T. Unravelling photoinduced interlayer spin transfer dynamics in two-dimensional nonmagnetic-ferromagnetic van der Waals heterostructures. *Nano Lett.* **21**, 3237 (2021).
- Li, T. et al. Pressure-controlled interlayer magnetism in atomically thin CrI₃. *Nat. Mater.* **18**, 1303 (2019).
- Yasuda, K., Wang, X., Watanabe, K., Taniguchi, T. & Jarillo-Herrero, P. Stacking-engineered ferroelectricity in bilayer boron nitride. *Science* **372**, 1458 (2021).
- Finney, N. R. et al. Tunable crystal symmetry in graphene–boron nitride heterostructures with coexisting moiré superlattices. *Nat. Nanotechnol.* **14**, 1029 (2019).
- Li, E. et al. Lattice reconstruction induced multiple ultra-flat bands in twisted bilayer WSe₂. *Nat. Commun.* **12**, 5601 (2021).

61. Thouless, D. J., Kohmoto, M., Nightingale, M. P. & den Nijs, M. Quantized Hall conductance in a two-dimensional periodic potential. *Phys. Rev. Lett.* **49**, 405 (1982).
62. Kohn, W. & Sham, L. J. Self-consistent equations including exchange and correlation effects. *Phys. Rev.* **140**, A1133 (1965).
63. Kresse, G. & Furthmüller, J. Efficient iterative schemes for ab initio total-energy calculations using a plane-wave basis set. *Phys. Rev. B* **54**, 11169 (1996).
64. Perdew, J. P., Burke, K. & Ernzerhof, M. Generalized gradient approximation made simple. *Phys. Rev. Lett.* **77**, 3865 (1996).
65. Grimmea, S., Antony, J., Ehrlich, S. & Krieg, H. A consistent and accurate ab initio parametrization of density functional dispersion correction (DFT-D) for the 94 elements H-Pu. *J. Chem. Phys.* **132**, 154104 (2010).
66. Xue, F., Wang, Z., Hou, Y., Gu, L. & Wu, R. Control of magnetic properties of MnBi_2Te_4 using a van der Waals ferroelectric In_2V_3 film and biaxial strain. *Phys. Rev. B* **101**, 184426 (2020).
67. Ma, X.-Y. et al. Large family of two-dimensional ferroelectric metals discovered via machine learning. *Sci. Bull.* **66**, 233 (2021).
68. Mostofi, A. A. et al. An updated version of wannier90: a tool for obtaining maximally-localised Wannier functions. *Comput. Phys. Commun.* **185**, 2309 (2014).

ACKNOWLEDGEMENTS

This work is supported by the National Natural Science Foundation of China (Nos. 11804190 and 12074217), Shandong Provincial Natural Science Foundation (Nos. ZR2019QA011 and ZR2019MEM013), Shandong Provincial Key Research and Development Program (Major Scientific and Technological Innovation Project) (No. 2019JZZY010302), Shandong Provincial Key Research and Development Program (No. 2019RKE27004), Shandong Provincial Science Foundation for Excellent Young Scholars (No. ZR2020YQ04), Qilu Young Scholar Program of Shandong University, and Taishan Scholar Program of Shandong Province.

AUTHOR CONTRIBUTIONS

W.D. executed calculations. W.D., R.P. and Z.H. performed data analysis. Y.M. supervised the project. W.D. and Y.M. co-wrote the paper. All authors discussed the results and commented on the manuscript at all stages.

COMPETING INTERESTS

The authors declare no competing interests.

ADDITIONAL INFORMATION

Supplementary information The online version contains supplementary material available at <https://doi.org/10.1038/s41699-022-00289-6>.

Correspondence and requests for materials should be addressed to Ying Dai or Yandong Ma.

Reprints and permission information is available at <http://www.nature.com/reprints>

Publisher's note Springer Nature remains neutral with regard to jurisdictional claims in published maps and institutional affiliations.



Open Access This article is licensed under a Creative Commons Attribution 4.0 International License, which permits use, sharing, adaptation, distribution and reproduction in any medium or format, as long as you give appropriate credit to the original author(s) and the source, provide a link to the Creative Commons license, and indicate if changes were made. The images or other third party material in this article are included in the article's Creative Commons license, unless indicated otherwise in a credit line to the material. If material is not included in the article's Creative Commons license and your intended use is not permitted by statutory regulation or exceeds the permitted use, you will need to obtain permission directly from the copyright holder. To view a copy of this license, visit <http://creativecommons.org/licenses/by/4.0/>.

© The Author(s) 2022